



193 nm ArF laser ablation and patterning of chitosan thin films

A. A. Aesa^{1,2} · C. D. Walton¹

Received: 15 November 2017 / Accepted: 15 May 2018 / Published online: 23 May 2018
© The Author(s) 2018

Abstract

This paper reports laser ablation studies on spin-coated biopolymer chitosan films, β -1,4-linked 2-amino-2-deoxy-D-glucopyranose. Chitosan has been irradiated using an ArF laser emitting at 193 nm. An ablation threshold of $F_T = 85 \pm 8 \text{ mJ cm}^{-2}$ has been determined from etch rate measurements. Laser-ablated chitosan is characterised using white light interferometry, scanning electron microscopy, and thermo-gravimetric analysis. Laser ablation of chitosan is discussed in terms of thermal and photoacoustic mechanisms. Heat transfer is simulated to assist in the understanding of laser-irradiated chitosan using a finite-element method and the software package COMSOL Multi-Physics™. As a demonstrator, a micro-array of square structures in the form of a crossed grating has been fabricated by laser ablation using a mask projection scanning method. The initial investigations show no evidence of thermal damage occurring to the adjacent chitosan when operating at a moderately low laser fluence of 110 mJ cm^{-2} .

1 Introduction

Laser ablation of bio-compatible and bio-degradable materials continues to be of great interest in a wide range of scientific and industrial areas [1]. One such material is chitosan, see Fig. 1. Chitosan is a natural polymer β -1,4-linked 2-amino-2-deoxy-D-glucopyranose that is used in medical applications and drug delivery [2, 3], antimicrobial [4], tissue engineering [5], and bio-medical applications [6–11], realisation of chitosan waveguides [12], and diffraction gratings [13]. Chitosan in the form of 2D and 3D scaffolds has been used in a wide range of applications [14]. Chitosan has been studied extensively for cell growth research in areas such as for the stabilization of platelets [15], utilization of chitosan scaffolds [16], laser patterning of bio-polymer substrates [10], and for controlling the growth direction of cells in bio-polymer materials [17]. In addition, chitosan has been used for the realisation of biosensors for the measurement of cholesterol levels [18] and for humidity sensors [19]. Several preparation methods are available, which include spin coating for thin film work [20, 21], casting methods [22], and

gravity-assisted drop-sphere techniques for producing spherical samples [22, 23]. There are also many methods used to pattern chitosan such as nano-imprint lithography, ion beam milling, and laser ablation processing. The latter is frequently selected as small features can be realised rapidly and over large areas. Laser processing of natural polymers is also of interest from a laser processing and light–matter interaction perspective. It is, therefore, of interest to understand the light–matter interaction processes as this will provide information as to which type laser is best-suited to process a specific material. With respect to laser processing of chitosan as is reported in this work, it is important to minimise thermal damage and denaturation. To the authors' knowledge, one of the first papers on excimer laser ablation of chitosan was carried out by Lazare et al. [24–26]. Similarly, a KrF laser emitting at 248 nm was used to study the ablation of collagen, chitosan, and PMMA [27]. More recently, Švorčík et al. have carried out laser ablation experiments at 248 nm on poly-L-lactic acid (PLLA) [28]. A comprehensive study on laser ablation of biological tissue was reported by Vogel and Venugopalan; see references within [11]. The complexities of laser material interaction associated with biological tissue were reported. Conclusion included work is importance in identifying laser-induced stress rates, denaturation kinetics, dynamics of tissue deformation, and fracture mechanisms. It was also concluded that further investigation could be carried out using longer laser wavelengths in the mid IR spectral region where absorption of radiation by

✉ A. A. Aesa
A.Aesa@2013.hull.ac.uk

¹ Department of Physics, School of Mathematics and Physical Sciences, University of Hull, Hull HU6 7RX, UK

² Department of Physics, College of Science, University of Kirkuk, Kirkuk, Iraq

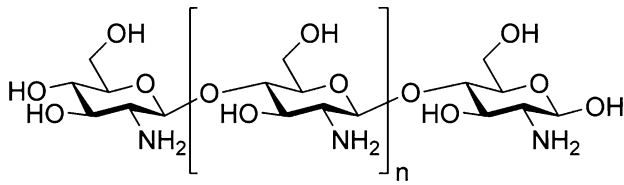


Fig. 1 Chemical structure of chitosan

water is significant. In addition, a comparative study was carried out using 193 and 248 nm to compare the interaction using comparable experimental parameters on two bio-polymers (poly-L-lactide and poly hydroxybutyrate) [29]. This work highlights the longer KrF 248 nm wavelength which penetrates deeper into the material and causes a significant bulk chemical modification verified using differential scanning calorimetry measurements. The study compared the former wavelength with shorter 193 nm radiation where the penetration of radiation is shorter. At this wavelength, one observes profound topological modifications and that surface chemical changes are less significant. Laser ablation resulted in foaming of the material in the irradiated region and the mechanism attributed to photoacoustic effects.

To the authors' knowledge, there appears to be less laser interaction studies on chitosan using ultra short femtosecond laser pulses. A femtosecond laser source has been carried out to pattern chitosan [30] and to study the fragmentation of laser-irradiated chitosan [31, 32]. A systematic study on the effects of pulse duration on the bio-polymers, starch, and chitosan, and their blends was carried out by Fotakis et al. [10]. A study was also carried out gelatine where foaming was observed using femtosecond and nanosecond lasers at wavelengths 213, 266, 400, and 800 nm [25, 33, 34]. This work reports experimental results of laser-ablated chitosan using an ArF laser emitting at a wavelength 193 nm.

2 Laser ablation

Lasers continue being used to study light–matter interactions of a wide range of materials. Ablation mechanisms vary and depend on the optical and material properties of a target material and on the specific laser parameters such as wavelength and photon energy. Laser ablation of polymers and biological tissue continues to be studied frequently with a wide range of applications in mind. Excimer lasers have been frequently used to ablate or desorb material from a target surface. Typically, optical absorption depths in the ultraviolet (UV) part of the electromagnetic spectrum tend to decrease with decreasing laser wavelength. Therefore, laser processing in the UV spectral region permits high-depth resolution. If the absorbed energy from a laser is rapidly

deposited, such that the heat does not have time to relax and diffuse out of the ablation volume, we have a condition called *thermal confinement*. This condition can be written in terms of the thermal diffusivity, χ , where the criterion for thermal confinement is that the laser pulse duration has to be shorter than a characteristic thermal relaxation time is given as follows:

$$\tau_{\text{th}} = \frac{d^2}{4\chi}, \quad (1)$$

where d is the shortest distance within the irradiated volume, either the spot size or the optical absorption depth. For many biological tissue and natural polymers, the thermal diffusivity is low (typically $\sim 10^{-8} \text{ m}^{-2} \text{ s}^{-1}$) and thermal denaturation is often minimal when using short laser pulses. Although only small amounts of material can be expelled from the surface of laser-irradiated polymeric materials, large acoustic stresses can be imparted due to recoil momentum [35]. Photomechanical mechanisms have been widely reported on laser ablation of biological tissue and polymeric materials [14]. The photoacoustic (PA) mechanism can take place when energy from a pulsed laser is rapidly transferred to a material [36]. The PA mechanism can be formally quantified in terms of the laser pulse duration, τ_p . If the laser pulse duration, τ_p , is shorter than the acoustic relaxation time, τ_{ac} , a condition of *stress or inertial confinement* can take place [37]. Stress confinement can be written in terms of these two parameters as $\frac{\tau_{\text{ac}}}{\tau_p} \geq 1$. Under this condition, an

irradiated material does not have sufficient time to reconfigure by changing its volume, and consequently, an increase in the internal pressure can occur. Under conditions of stress confinement, a compressional wave develops into a tensile wave, and molecular bonds can be weakened and break. Because stress waves can result in material damage without imparting a significant thermal damage, the ablation process is referred to as *cold ablation*. We can write a condition for stress confinement in terms of the speed of the stress wave, c_s , as follows:

$$\frac{l_{\text{ac}}}{l_{\text{opt}}} = \frac{c_s \tau_p}{\alpha^{-1}} = \alpha c_s \tau_p < 1, \quad (2)$$

where l_{opt} is the optical penetration depth and l_{ac} is the distance travelled by the acoustic wave propagating inside an irradiated material. When the above equation is satisfied changes in the internal pressure become significant. Therefore, absorption of short laser pulses, τ_p , in materials that have moderate absorption coefficients, α , can lead to photomechanical ablation. We note that the absorption of optical radiation and material properties is sensitive to the concentrations and preparation methods. Therefore, in this work, experiments are carried out on samples that have had equal

drying times before the laser ablation experiments were conducted. As the energy from the laser pulse is deposited inside a target material, a compressional stress wave propagates in both the $\pm z$ directions normal to the sample surface where the positive $+z$ direction is designated as the beam propagates direction. Similarly, a compressional wave propagates in the opposite $-z$ direction towards the free surface of the sample. At the free surface, there is, in general, a high acoustic reflection coefficient at the air–material interface and the acoustic stress wave is reflected back into the bulk of the sample in the $+z$ direction. As the compressional wave relaxes, a tensile stress wave builds up and propagates back into sample. The magnitude of the tensile stress increases with depth into the bulk of the material before decaying away. Such tensile stresses may lead to bond breakage, cavity formation, and bubble nucleation. In some cases, depending on the laser fluence, heat may also be generated and lead to laser-induced material damage. For an isotropic solid, the laser-induced stresses can be described by a general stress–strain tensor, shown as follows [38]:

$$\sigma_{ik} = \frac{3B}{1 + \sigma} [(1 - 2\sigma)\epsilon_{ik} + \sigma\epsilon_{ik}\delta_{ik}] - B\beta\Delta T\delta_{ik}, \tag{3}$$

where E is Young’s modulus, σ (without subscripts) is the Poisson ratio, ϵ_{ij} are the induced strains, and δ_{il} is the Kronecker delta function. The stress–strain tensor takes on negative and positive signs for tensile and compressive stresses, respectively. The last term in the stress–strain tensor, $B\beta\Delta T\delta_{ij}$, corresponds to the maximum stress. A relative change in volume can be written in terms of the strains as $\frac{V}{\Delta V} = \epsilon_{kk} = \epsilon_{11} + \epsilon_{22} + \epsilon_{33}$. On absorption of a short duration laser pulse, and if $\epsilon_{kk} = 0$, the condition of stress confinement is obeyed. In this context, short laser pulses refer to the laser pulse duration being less than the acoustic transit time, $\tau_p \ll \tau_{ac} = \frac{d}{c_s}$, where d is the shortest distance in the irradiated volume. The circular geometry and axial symmetry of the ablation sites used in this work is suited for the use of polar coordinates. In many laser ablation experiments, there are cases where the radial stresses, σ_{rr} , and circumferential stresses, $\sigma_{\phi\phi}$, become significant and contribute to laser-induced damage [39]. Although the magnitude of circumferential stresses is smaller than longitudinal stresses, circumferential (Hoop) stresses can exist for extended lifetimes and, therefore, become play a significant role in laser-induced damage. As radial stresses are induced inside an ablation crater, the expanding material can push material outwards inducing circumferential tensile stresses in the region outside of the ablation crater [40]. Expressions for the radial and circumferential stresses, respectively, are shown as follows:

$$\sigma_{rr} = \frac{E}{1 + \sigma} \left(\frac{\partial^2 \phi}{\partial r^2} - \nabla^2 \phi \right), \tag{4a}$$

$$\sigma_{\phi\phi} = \frac{E}{1 + \sigma} \left(\frac{1}{r} \frac{\partial \phi}{\partial r} - \nabla^2 \phi \right), \tag{4b}$$

where ϕ is the thermo-elastic displacement potential [41]. These stresses can become important considerations especially when laser beams have circular symmetry and when using circular object masks. An equation for thermo-elastic wave written in terms of the velocity potential, ϕ , is shown as follows [42].

$$\nabla^2 \phi - \frac{1}{c_s^2} \frac{\partial^2 \phi}{\partial t^2} = \frac{\beta}{\rho C} S, \tag{5}$$

where S is a heat source term per unit time and volume, and C is the specific heat capacity. From the velocity potential, one obtains the velocity by taking the gradient of ϕ :

$$v = \text{grad}\phi, \tag{6}$$

and by taking the partial derivative of ϕ , one obtains the pressure as shown in the following:

$$P = -\rho \left(\frac{\partial \phi}{\partial t} \right). \tag{7}$$

The pressure developed inside a target depends on the relative volume change plus any addition of a change in the material temperature and we can write the over pressure as follows:

$$P = -\beta \frac{\Delta V}{V} + B\beta\Delta T, \tag{8}$$

where β is the volume expansion coefficient, V is the volume of the irradiated material, B is the bulk modulus, and T is the corresponding temperature of the material. Of relevance in this work is to estimate the pressure a laser fluence F as shown in the following:

$$P = \pm \frac{\beta AF}{C_p \alpha \tau_p^2} (1 - e^{-\alpha z}), \tag{9}$$

where A is the absorptivity $(1 - R)$, where R is the optical reflectivity of the material at the corresponding wavelength, and the remaining parameters have been defined earlier. We note, when energy is rapidly deposited by a laser pulse, the tensile stress evolves. In this work, we simulate an acoustic wave propagating inside chitosan using an approach as previously reported [20, 22]:

$$P_0(z, t) = P_1 + P_2 + P_3, \tag{10}$$

$$P_1(z, t) = 0.5P_{\max} e^{-\alpha(z-c_s t)} \quad z > c_s t \quad z > c_s t, \tag{11}$$

$$P_2(z, t) = 0.5P_{\max} e^{-\alpha(z+c_s t)} \quad z > 0, \tag{12}$$

$$P_3(z, t) = 0.5P_{\max} R_s e^{-\alpha(c_s t - z)} \quad c_s t > z > 0, \tag{13}$$

where the maximum pressure, $P_{\max} = \Gamma \alpha F$, can be written in terms of the laser fluence, F , the absorption coefficient, α , and the Gruneisen coefficient, $\Gamma = \left(\frac{\partial \ln P}{\partial \ln U/V} \right)_V$, where U and V are the internal energy and volume, respectively. $R_s = \frac{Z_{\text{air}} - Z_{\text{chit}}}{Z_{\text{air}} + Z_{\text{chit}}}$, which is the reflectivity of the acoustic wave, and $Z = \rho c_s$ is the acoustic impedance of air and chitosan. The resulting pressure wave $P_T(z, t)$ can be found by carrying out a convolution of the acoustic wave with the temporal laser pulse $g(t)$ and is written as follows:

$$P_T(z, t) = g(t) \otimes P_0(z, t), \quad (14)$$

$$P_T(z, t_2) = \int_0^{t_2} g(t_1) P_0(t_2 - t_1) dt_1. \quad (15)$$

The laser pulse used in the simulations is represented by $g(t)$ and the function closely resembles the ArF 193 nm excimer laser pulse used in these experiments:

$$g(t) = t^2 e^{-\frac{t}{\tau}} \left(\int_0^{\infty} t^2 e^{-\frac{t}{\tau}} dt \right)^{-1}. \quad (16)$$

In this work, the laser pulse duration $\tau_p = 11.5$ ns FWHM. The simulation was implemented using MatLAB. In the simulations presented here, positive and negative values correspond to compression and tensile stress, respectively.

3 Temperature calculations

Calculations of the temperature rise of laser-irradiated chitosan have been undertaken using a finite-element method (FEM) using the software COMSOLTM version 5.3. The default solver settings were used for time-dependent heat transfer studies with the exception of the time stepping which was set to strict. This forces the code to solve at each of the manually defined individual time steps with the solver taking any necessary intermediate steps. A triangular mesh was selected and the simulations included temperature-dependent properties. A three-layer geometry was implemented consisting of air at the front surface of a chitosan sample that was supported on a soda–lime glass substrate. As will be shown, the substrate significantly affects the temperature due to heat sink effects. Finally, the experimentally measured temporal pulse shape (11.5 ns FWHM) was incorporated in the temperature simulations.

4 Experimental

Laser ablation experiments were carried out using a Lambda Physik LPF 202 laser emitting at a wavelength of 193 nm. A stainless steel circular object mask of 2 mm diameter was positioned in a uniform part of the raw laser beam. The aperture was imaged onto the free surface of the chitosan using a 1/10 \times magnification. Scanning electron micrographs and energy-dispersive X-ray measurements were carried out using a scanning electron microscope (SEM) (model, Zeiss EVO60). AFM measurements were carried out using the non-contact tapping mode (Model, Bruker edge). Samples were mounted on a motion control stage (Aerotech, Fibre Align). The laser output passed through a dual rotating plate attenuator (MetroLux, ML2110) to control the laser fluence. Dielectric mirrors optimised for transmission at 45 $^\circ$ were used to steer the beam, such that the beam was incident from the vertical and normal to the chitosan surface. The output energy of the laser was measured after all optical components using a Joule meter (Molelectron). The laser pulse duration was measured using a fast photo diode (Hamamatsu, S7911) connected to an oscilloscope (Infinium, 500 MHz, 2 GB samples s⁻¹).

Thin films of chitosan (Sigma-Aldrich, Chitosan-448869) were spin-coated, (Oscilla) onto soda–lime glass microscope slides (Thermo Scientific). Calibration curves were carried out to identify the spin speed for samples having thicknesses in the range 500 nm to 10 μ m. The chitosan solution was prepared by dissolving 0.2 mg chitosan in 10 mL acetic acid to achieve a 2% (w/v) concentration. A mass of 0.2 mg was placed in the 10 mL of acetic acid and agitated using a magnetic stirrer for 5 h until the chitosan was fully dissolved. The samples were then coated and left to dry for 1 day before carrying out the laser ablation experiments.

Samples were prepared on aluminium stubs and coated with carbon by the thermal evaporation of graphite under vacuum (Model: E12E series). The SEM stubs were located onto 32 mm-diameter steel planets and placed on a rotary table in the coating chamber, and the pressure pulled down to ($\sim 10^{-5}$ Torr). The planets were oriented at 45 degrees to the carbon source and separated by a distance of about 25 cm. The planets were rotated at one revolution per second and a coating of approximately 5 nm was applied.

5 Results and discussion

Figures 2, 3 show FEM simulations of the calculated temperature rise for chitosan that has been irradiated using a laser fluence of 85 and 760 mJ cm⁻², respectively. At the

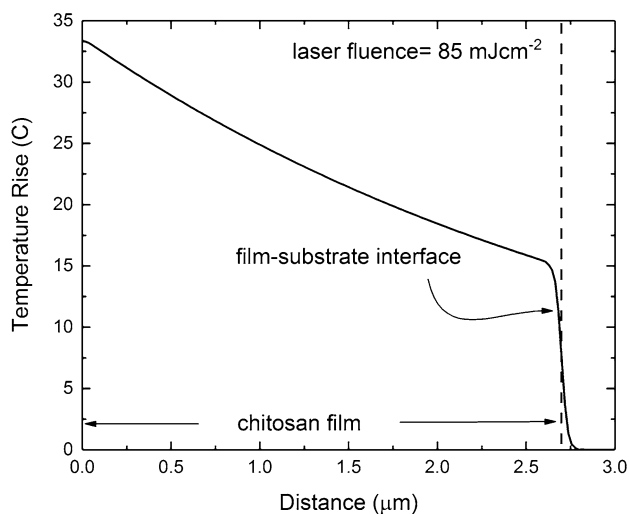


Fig. 2 Surface temperature rise of chitosan simulated using COMSOL 5.3. Chitosan was irradiated at a laser fluence of 85 mJ cm^{-2} , laser pulse duration, $\tau_p = 11.5 \text{ ns}$ FWHM

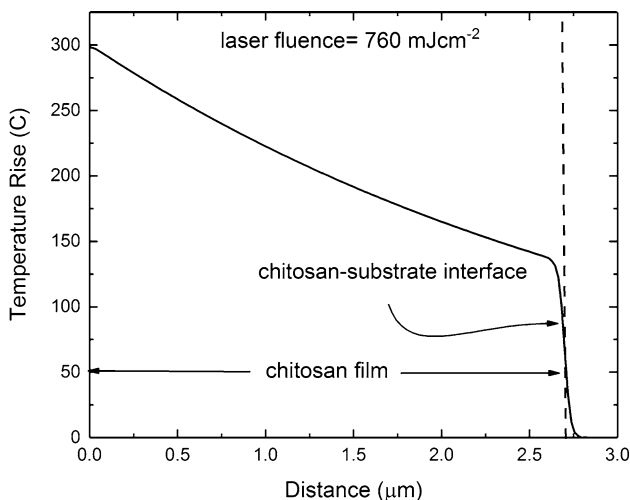


Fig. 3 Surface temperature rise of chitosan simulated using COMSOL 5.3. Chitosan was irradiated at laser fluence of 760 mJ cm^{-2} , $\tau_p = 11.5 \text{ ns}$ FWHM

lower laser fluence, the temperature rise is relatively low, at $\sim 33 \text{ }^\circ\text{C}$. At a higher laser fluence of 760 mJ cm^{-2} , there is a concomitant increase in the temperature rise reaching $\sim 300 \text{ }^\circ\text{C}$ at the front surface of the chitosan. In both cases, heat sink effects are observed as heat is being transferred through the glass substrate resulting in a more rapid decrease in the temperature at the chitosan–substrate interface. At the lower fluence, the temperature rise is lower than the glass transition of chitosan [44, 45], whereas, at the higher laser fluence, the opposite is true. UV–Vis absorption measurements were carried out on dried chitosan films; see Fig. 4. As can be seen, the absorption

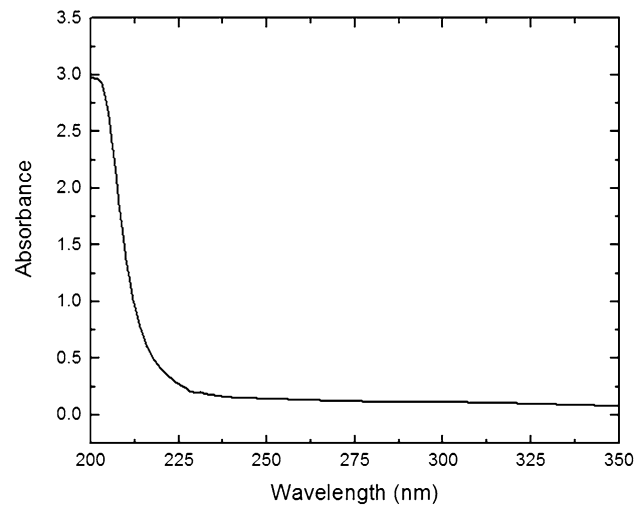


Fig. 4 UV–Vis absorption spectra of chitosan film

increases towards the UV spectral region. The graph shows an average of five absorption measurements for 2% concentration (w/v) of chitosan mixed with acetic acid. The spectra indicates that chitosan thin films are optically transparent over a broad range of the visible spectrum. At shorter wavelengths, around 225 nm, the optical absorption increases rapidly. From these measurements, an average absorption coefficient of $\alpha_{\text{Spec}} = 3 \pm 0.3 \times 10^3 \text{ cm}^{-1}$ was determined. In many applications, it is prudent to minimise thermal damage induced during laser processing for example, and therefore, it is important to select a low laser fluence to avoid damage to the surrounding material. We note that the thermal diffusivity of chitosan is low and heat flow is of the order of $L_H = 4\sqrt{\chi\tau_p} = 120 \text{ nm}$. Therefore, establishing an ablation threshold at 193 nm becomes important. Etch rate measurements have been carried out to determine the laser ablation threshold, F_T , and the results are shown in Fig. 5. A set of experiments were conducted over a laser fluence between 70 mJ cm^{-2} to a maximum of 4.5 J cm^{-2} . Etch depths were established by measuring the depths of the ablation craters using a WLI. Etch depths were deduced from five experiments carried out at different locations of the sample for each laser fluence. From the measurements, an ablation threshold of $F_T = 85 \pm 8 \text{ mJ cm}^{-2}$ was determined. Ablation etch rates close to F_T are relatively low at a nanometre per pulse level. At the higher laser fluence, the etch rates were beginning to plateau. This can be assigned to several effects, photon shielding by ablation products, and surface re-structuring causing the effective surface area to increase. We suggest that the effective surface area is increasing as laser-driven acoustic wave induces tensile stresses and bubbles nucleate modifying the surface topology. Photoacoustic studies of tissue ablation have been

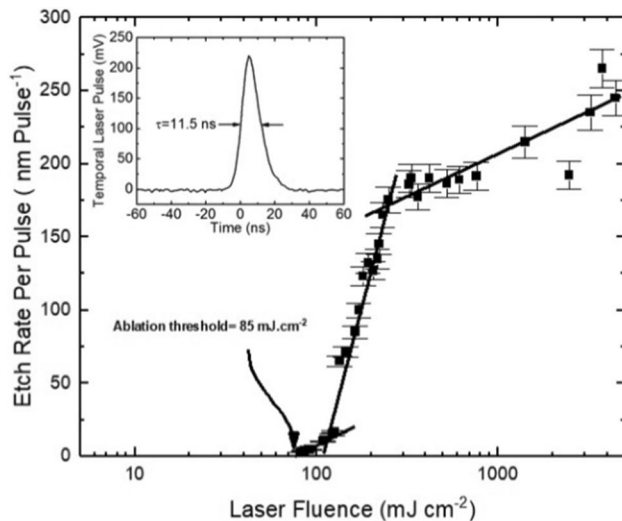


Fig. 5 Etch rate measurements of laser-ablated chitosan at a wavelength of 193 nm. The inset shows the measured temporal laser pulse, $\tau_p = 11.5$ ns FWHM

previously reported [46, 47]. In some cases, laser ablation has resulted in the formation of bubbles and foaming at the surface of the irradiated site [24, 25, 48]. The experimentally determined ablation threshold was compared with a simple thermal energy balance equation:

$$\alpha A F_{\text{evap}} = \rho [C(T_b - T_0) + L_v], \quad (17)$$

where C is the specific heat capacity, T_b and T_0 are the boiling temperature and initial temperature, respectively, ρ is the density, and L_v is the latent heat of vaporisation. Using the corresponding values, a laser ablation threshold of $F_{\text{evap}} = 900 \text{ mJ cm}^{-2}$ is calculated [25, 49]. This is close to a tenfold higher value of the ablation threshold compared with etch rate experiments. This calculation and SEM measurements of the ablated chitosan samples presented here prompts one to investigate alternative ablation mechanisms to describe the ablation process. The photoacoustic (PA) mechanism can play a significant role in laser ablation, especially in polymeric materials and biological tissue [24, 43]. Figure 6a shows an SEM micrograph of a circular ablation crater that was produced by applying a laser fluence of 125 mJ cm^{-2} . This fluence is above but close to the ablation threshold and one observes localised blistering on the surface. Figure 6b shows a magnified image of the blistered region. The blistering is suggestive of sub-surface volumetric expansion due to gaseous species expanding from beneath the surface. In an attempt to select a uniform photon flux a circular object mask, 2 mm diameter was positioned centrally in the Hermite–Gaussian beam of the ArF laser beam. We suggest two possibilities for the appearance of localised blistering. Random, spatially distributed intensity fluctuations within the beam can occur [50]. These intensity

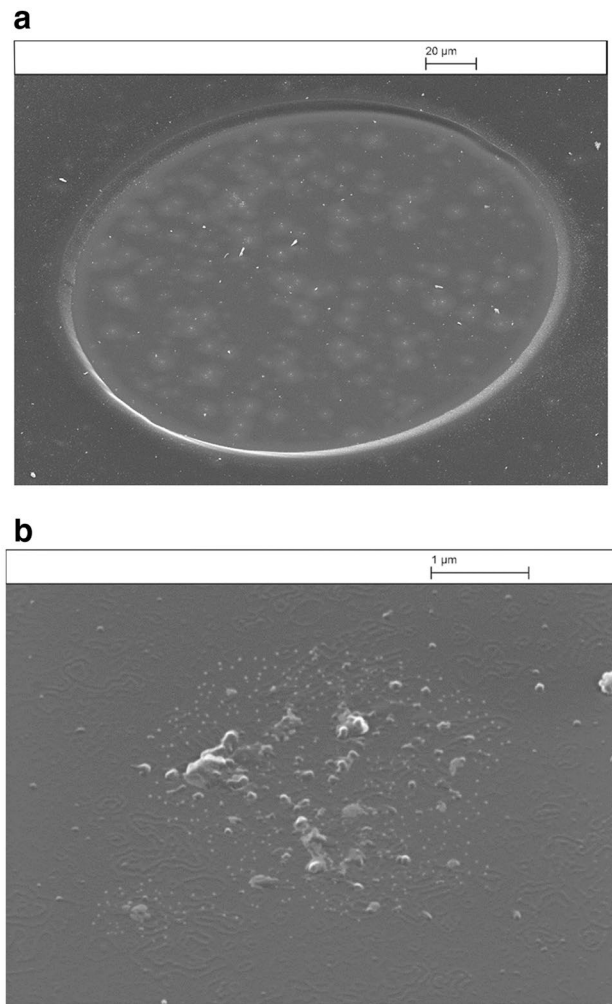


Fig. 6 **a** SEM image of chitosan thin film in thickness of $2.7 \mu\text{m}$ irradiated with 193 nm laser, imaged in $\times 10$ magnification, repetition rate 1 Hz, 10 laser pulses, laser fluence 125 mJ cm^{-2} , depth 185 nm per pulse, circle mask in size of 2 mm, tilt angle 45° , and at a magnification of 1.6 k. **b** Same parameters as above and at a $\times 60$ k magnification

fluctuations will manifest in hotspots within the beam that are projected onto the near surface of the sample. The influence of hot spots may heat the chitosan at the surface and down the optical absorption depth α^{-1} and the hotspots may drive gaseous expansion. An alternative description may be due to incomplete mixing of the solvent during the sample preparation stage which may introduce different degrees of optical absorption. Similarly, a combination of these two effects could exist. However, Gaining a deeper understanding of the mechanism associated with blistering requires further work. Figure 7a shows an ablation site under the same imaging condition as the previous results but at an increased laser fluence of 250 mJ cm^{-2} . The surface topology has changed significantly from the lower laser fluence. Figure 7b shows an SEM of a magnified region within the

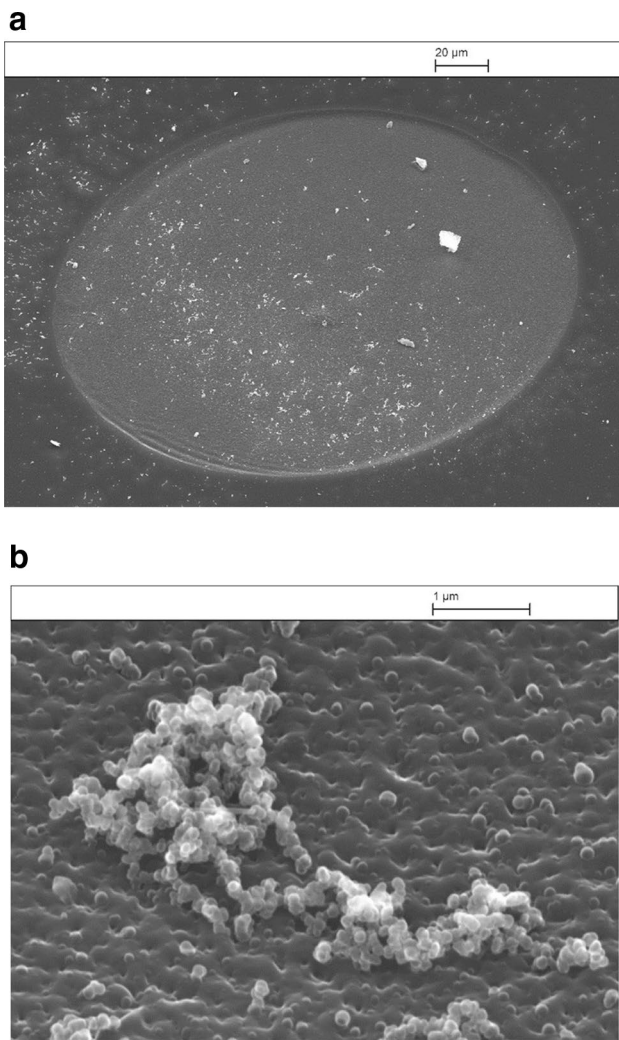


Fig. 7 **a** SEM image of chitosan thin film in thickness of $2.7 \mu\text{m}$ irradiated with 193 nm laser, imaged in $\times 10$ magnification, repetition rate 1 Hz, 10 laser pulses, laser fluence 250 mJ cm^{-2} , depth 17 nm per pulse, circle mask of 2 mm diameter, 45° tilt angle, and $\times 1.6 \text{ k}$ magnification. **b** Centre of the laser ablation crater at 60 k magnification

floor of the same crater. Evidence of foaming is seen to be growing from the near surface. Foaming has been reported to occur during laser ablation of collagen and other bio-polymers using a KrF laser emitting at a wavelength of 248 nm [24, 51]. Foaming of collagen and chitosan was described in terms of cavitation effects induced by photoacoustic stresses. In the results presented in this work, the regions of localised foaming consist of spherical globules that appear to be penetrating the surface of the chitosan. The formation of spherical features and the nucleation of bubbles is suggestive of tensile stresses causing voids within the chitosan. A simple model, implemented using MatLAB, using Eqs. (10)–(16) has been used to simulate the propagation of a laser-generated stress wave in a material that has a free surface. Figure 8 shows the simulated photoacoustic wave propagating

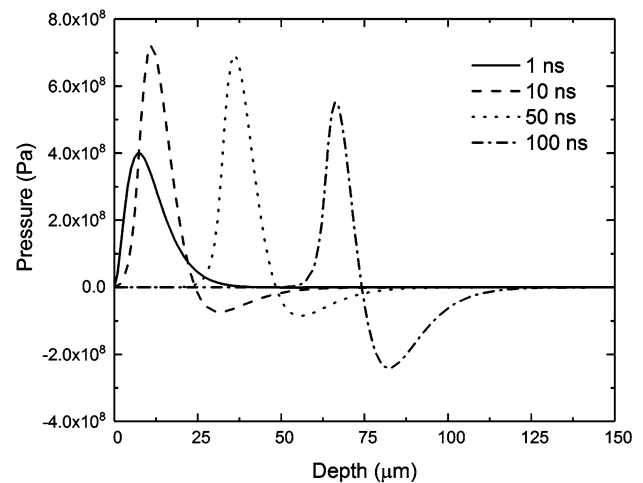


Fig. 8 Simulated photoacoustic stress wave using MatLAB. Positive values correspond to compressive stresses and negative values are tensile stresses. The different curves correspond to times: 1, 10, 50, and 100 ns. The laser pulse is 11.5 ns FWHM and a Gruneisen coefficient of $\Gamma = 1$. Laser fluence of 760 mJ cm^{-2}

in a planar film at different times after absorption of a laser pulse. Figure 8 is simulated for the material chitosan and at a corresponding laser fluence of 760 mJ cm^{-2} . A tensile stress corresponds to a negative value, and conversely, a positive value corresponds to a compressive stress. As can be seen, a tensile stress increases as the acoustic wave propagates with depth into the chitosan sample. To further investigate the results of surface modification, we turned our attention to the decomposition of chitosan. Figure 9 shows AFM images of the surface topology of (a) un-irradiated chitosan film and laser-irradiated chitosan film at a fluence of (b) 80, (c) 135, and (d) 760 mJ cm^{-2} corresponding to average surface roughness, $R_a \sim 32, 45, \text{ and } 110 \text{ nm}$, respectively. The topography of the un-irradiated and laser-irradiated samples at the low fluence (80 mJ cm^{-2}) is very similar. At a laser fluence of 135 mJ cm^{-2} , some bubbling is observed. The bubbling and cavity formation is unevenly distributed over the chitosan surface and R_a values vary over the measured area of $50 \times 50 \mu\text{m}^2$. At the high fluence of 760 mJ cm^{-2} , there is a concomitant increase in the density of foaming and cavities. Figure 9d indicates signs of strain on the surface which may be explained by chitosan having a negative thermal expansion coefficient. Figure 10 shows the results of energy-dispersive X-ray (EDX) measurements of un-irradiated and laser-irradiated chitosan at a laser fluence of 80 and 760 mJ cm^{-2} . Three peaks are observed: carbon, nitrogen and oxygen at energies of 0.27, 0.4 and 0.52 keV, respectively. To quantify the degree of chemical change between the un-irradiated and irradiated chitosan, we measure the counts ratio between the oxygen and nitrogen peaks, namely, 15.8, 21.2, and 39.0 for un-irradiated and when irradiated

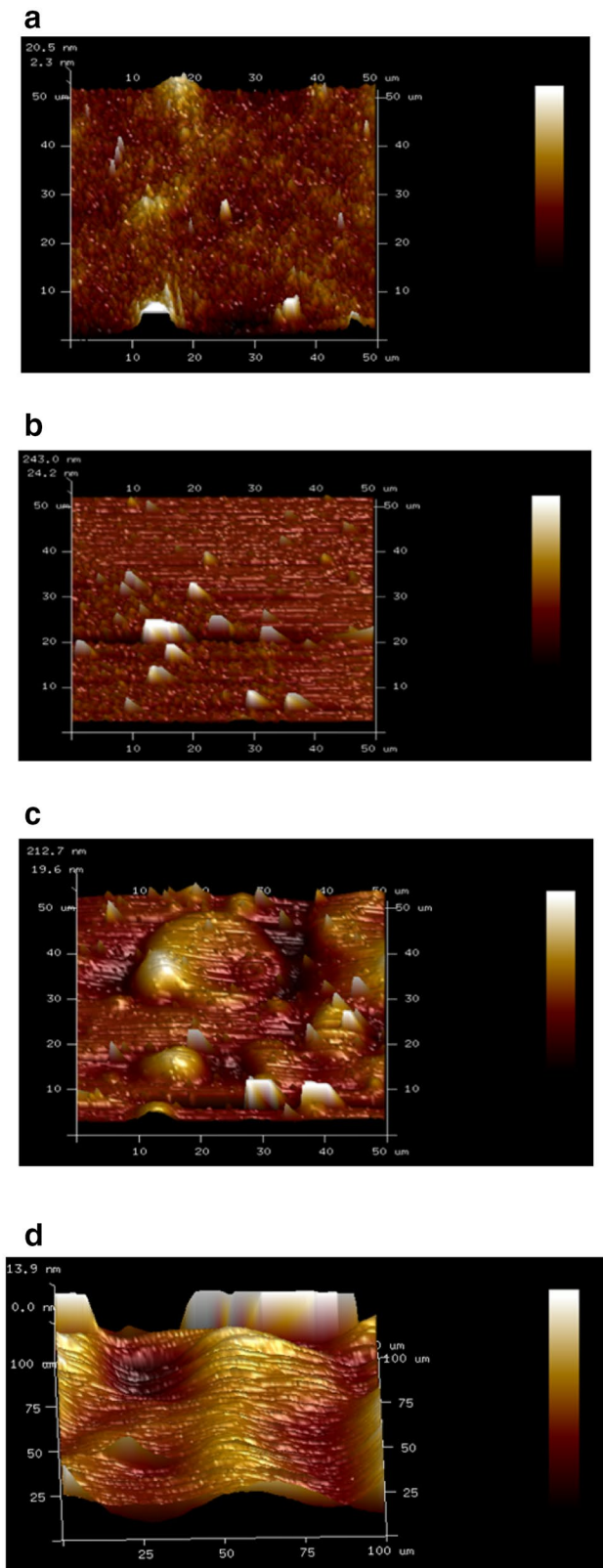


Fig. 9 AFM image of chitosan **a** un-irradiated and laser-irradiated using a 1/10 magnification and a pulse repetition frequency of 1 Hz. **b** 80 mJ cm⁻², **c** 135 mJ cm⁻², and **d** 750 mJ cm⁻²

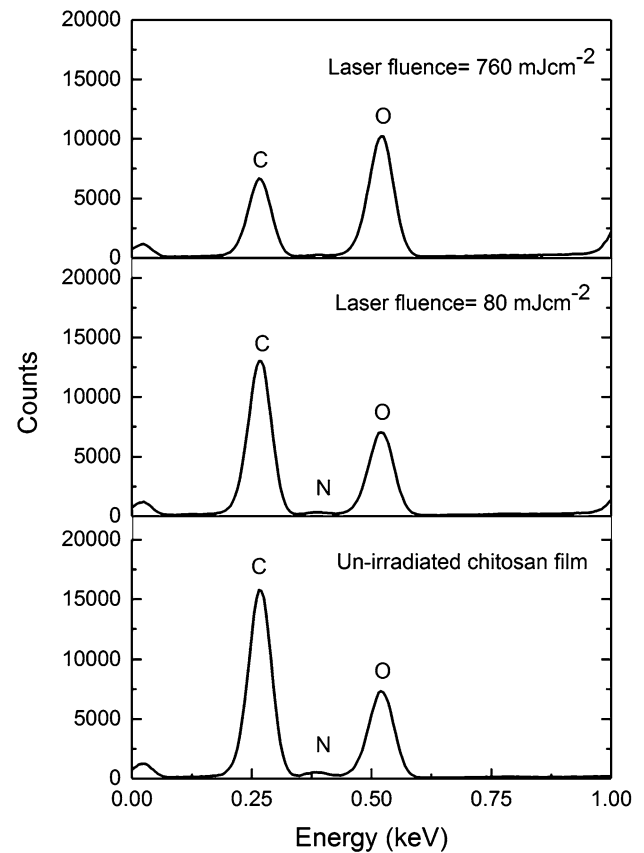


Fig. 10 Energy-dispersive X-ray (EDX) measurements of chitosan for un-irradiated (bottom) and irradiated at a laser fluence of 80 mJ cm⁻² (middle) and 760 mJ cm⁻² (top)

at 80 and 760 mJ cm⁻², respectively. At the low laser fluence, both the oxygen and nitrogen peaks decrease when irradiated. At the higher laser fluence, the oxygen content increases substantially and the nitrogen peak decreases. From these results, it may be prudent to laser process chitosan as close as possible to the ablation threshold to prevent any chemical denaturation of chitosan at a wavelength of 193 nm.

Measuring the glass transition temperature of chitosan is challenging due to its hydrophilic nature and the vast number of blends that can be used. Because of this there is spread in values for a glass transition temperature. Typical values for the glass transition temperature are between 59 and 158 °C [52, 53]. A sample of chitosan was prepared under the same conditions as those samples used for ablation studies. The prepared samples were used to measure the decomposition of chitosan using thermo-gravimetric analysis (TGA) and the results are shown in Fig. 11. From the derivative, we observe and discuss two peaks. A glass transition temperature $T_g = 152$ °C and a decomposition temperature $T_d = 300$ °C. A careful study on the glass decomposition temperature of chitosan has been reported by Sakurai et al., reporting

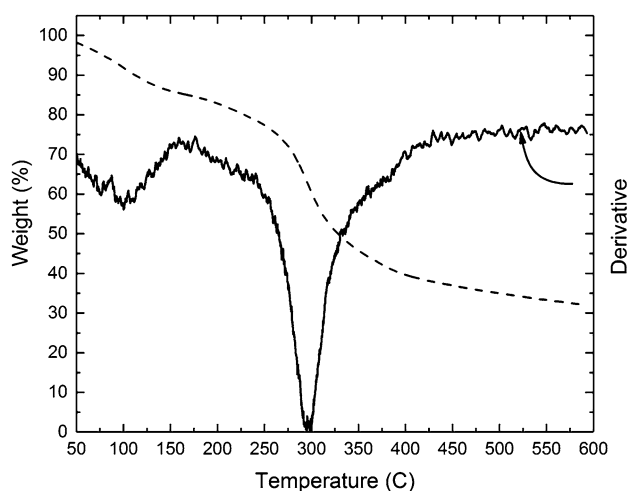


Fig. 11 Thermogravimetric analysis (TGA) 2% (w/v) chitosan in acetic acid. The dotted line is the TGA measurement and the solid line is the derivative of the measurement. Two peaks are observed: a glass transition and a decomposition temperature of $T_g = 158$ °C and $T_d = 300$ °C, respectively

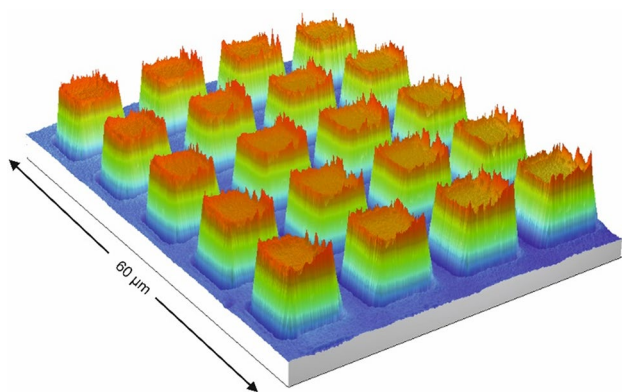


Fig. 12 White light Interferometric (WLI) measurement of laser-irradiated chitosan. The square structures are $10 \mu\text{m}^2$ and 525 nm high. The structure was produced by mask projection and translating the sample relative to the beam using a laser fluence 110 mJ cm^{-2} , at a pulse repetition frequency of 10 Hz, a stage velocity of 0.1 m ms^{-1} and receiving 40 overlapping laser pulses

a glass transition temperature for chitosan of $T_g = 203$ °C [45]. Similarly, Dong et al. have used four techniques to measure the glass transition temperature of chitosan and a glass transition temperature in the range $T_g = 140$ – 150 °C has been reported. The spread in the results illustrates the effects of the many parameters that need to be considered when preparing solvent-based samples. To demonstrate the patterning capabilities of chitosan, we report a structure that was fabricated by ablating chitosan. Figure 12 shows a WLI image of a 2D cross-grating structure realised in chitosan. The patterned chitosan consists of laser-patterned crossed

grating 5×5 mm. Figure 12 shows a magnified image of the grating that consists of a 5×4 array of square features. A thin film of chitosan was spun onto a microscope slide and the chitosan was laser-ablated to reveal the underlying carrier substrate. Each structure is 525 nm high and was produced using simple mask dragging technique. The sample was translated relative to the laser beam that imaged a parallel bar object mask onto the free surface of the chitosan. After scanning in one direction, the sample was rotated and the scanning process was repeated to achieve the square features. On inspection of the chitosan, there is a little evidence of thermal damage to the square chitosan features. This may be attributable to the low laser fluence of 110 mJ cm^{-2} , the short laser pulse duration, and the low value of thermal diffusivity in chitosan. The ability to laser pattern chitosan, and other natural polymers, may open up new avenues for the utilization of bio-compatible and bio-degradable devices.

6 Conclusion

In conclusion, spin-coated films of chitosan have been irradiated using an ArF laser emitting at a wavelength of 193 nm. An ablation threshold at 193 nm of $85 \pm 8 \text{ mJ cm}^{-2}$ is measured. TGA results show thermal decomposition of chitosan taking place at ~ 300 °C. Laser ablation of chitosan at a laser fluence close to the ablation threshold shows minimal sign of thermal damage to the adjacent chitosan. At elevated laser fluence, the base of the ablation crater shows the evidence of damage and bubble formation taking place. The damage is tentatively explained as being due to a combination of thermal and photomechanical mechanisms taking place giving rise to weakening of bonds and nucleation of cavities and bubble formation. High optical absorption permits controlled depth resolution close to the ablation threshold of typically ~ 5 nm per pulse at a wavelength of 193 nm. AFM results conform that surface roughness increases with laser fluence and the average surface roughness is at a nanometer level near the onset of surface modification. EDX measurements indicate that the chemical composition is unchanged when irradiated at a fluence that is close to the ablation threshold. Thermal damage is minimal when chitosan is irradiated close to the ablation threshold as the induced temperature rise is also low. Laser processing of chitosan at a laser fluence close to the ablation threshold may open up novel fabrication routes for the realisation of bio-compatible and bio-degradable optical devices for sensing applications.

Acknowledgements We acknowledge the Ministry of Higher Education & Scientific Research, Iraq, for supporting Abdulsattar Aesa for a Ph.D. at the University of Hull. We would like to thank the Iraqi Cultural Attaché, London, for their support. Mr. A. Sinclair is also thanked for the SEM measurements.

Open Access This article is distributed under the terms of the Creative Commons Attribution 4.0 International License (<http://creativecommons.org/licenses/by/4.0/>), which permits unrestricted use, distribution, and reproduction in any medium, provided you give appropriate credit to the original author(s) and the source, provide a link to the Creative Commons license, and indicate if changes were made.

References

- M. Rinaudo, *Prog. Polym. Sci.* **31**, 603 (2006)
- V. Bansal, P.K. Sharma, N. Sharma, O.P. Pal, R. Malviya, *Biol. Res.* **5**, 28 (2011)
- V.R. Sinha, A.K. Singla, S. Wadhawan, R. Kaushik, R. Kumria, K. Bansal, S. Dhawan, *Int. J. Pharm.* **274**, 1 (2004)
- E.I. Rabea, M.E.T. Badawy, C.V. Stevens, G. Smagge, W. Steurbaut, *Biomacromol.* **4**, 1457 (2003)
- F. Croisier, C. Jérôme, *Eur. Polym. J.* **49**, 780 (2013)
- I. Michaljaničová, P. Slepíčka, M. Veselý, Z. Kolská, V. Švorčík, *Mater. Lett.* **144**, 15 (2015)
- I. Michaljaničová, P. Slepíčka, S. Rimpelová, N. Slepíčková, Kasálková, V. Švorčík, *Appl. Surf. Sci.* **370**, 131 (2016)
- P. Slepíčka, I. Michaljaničová, S. Rimpelová, V. Švorčík, *Mater. Sci. Eng. C* **76**, 818 (2017)
- P. Slepíčka, N.S. Kasalkova, J. Siegel, Z. Kolska, L. Bacakova, V. Švorčík, *Biotechnol. Adv.* **33**, 1120 (2015)
- M. Castillejo, E. Rebollar, M. Oujja, M. Sanz, A. Selimis, M. Sigletou, S. Psycharakis, A. Ranella, C. Fotakis, *Appl. Surf. Sci.* **258**, 8919 (2012)
- A. Vogel, V. Venugopalan, *Chem. Rev.* **103**, 577 (2003)
- S.S. Voznesenskiy, A.A. Sergeev, A.Y. Mironenko, S.Y. Bratskaya, Y.N. Kulchin, *Sens. Actuators B Chem.* **188**, 482 (2013)
- C.S. Camilo, D.S. dos Santos, J.J. Rodrigues, M.L. Vega, S.P. Campano Filho, O.N. Oliveira, C.R. Mendonça, *Biomacromolecules* **4**, 1583 (2003)
- I.Y. Kim, S.J. Seo, H.S. Moon, M.K. Yoo, I.Y. Park, B.C. Kim, C.S. Cho, *Biotechnol. Adv.* **26**, 1 (2008)
- K. Baysal, A.Z. Aroguz, Z. Adiguzel, B.M. Baysal, *Int. J. Biol. Macromol.* **59**, 342 (2013)
- Y. Zhang, M. Zhang, *J. Mater. Sci. Mater. Med.* **15**, 255 (2004)
- E.A. Bremus-Koebberling, S. Beckemper, B. Koch, A. Gillner, *J. Laser Appl.* **24**, 42013 (2012)
- C.B. Mathews, T.M. Libish, B. Kaushalkumar, V. Vivek, R. Prabhu, P. Radhakrishnan, *Optoelectron. Lett.* **12**, 23 (2016)
- A. Sergeev, S. Voznesenskiy, *Opt. Mater. (Amst)*. **43**, 33 (2015)
- W.H. Nosal, D.W. Thompson, L. Yan, S. Sarkar, A. Subramanian, J.A. Woollam, *Colloid. Surf. B Biointerfaces* **43**, 131 (2005)
- A.L. Da Róz, F.L. Leite, L.V. Pereiro, P.A.P. Nascente, V. Zucolotto, O.N. Oliveira, A.J.F. Carvalho, *Carbohydr. Polym.* **80**, 65 (2010)
- R. Lieder, M. Darai, G. Orlygsson, O.E. Sigurjonsson, *Biol. Proc. Online* **15**, 11 (2013)
- S. Li, Z. Wu, B. Li, R. Zhu, Y. Wang, *Water Sci. Technol.* **66**, 2461 (2012)
- S. Lazare, V. Tokarev, A. Sionkowska, M. Wiśniewski, *Appl. Phys. A Mater. Sci. Process.* **81**, 465 (2005)
- S. Lazare, R. Bonneau, S. Gaspard, M. Oujja, R. de Nalda, M. Castillejo, A. Sionkowska, *J. Laser Micro Nanoeng.* **4**, 152 (2009)
- S. Lazare, R. Bonneau, S. Gaspard, M. Oujja, R. de Nalda, M. Castillejo, A. Sionkowska, *Appl. Phys. A Mater. Sci. Process.* **94**, 719 (2009)
- S. Lazare, V.N. Tokarev, A. Sionkowska, M. Wiśniewski, *J. Phys. Conf. Ser.* **59**, 543 (2007)
- P. Slepíčka, I. Michaljaničová, P. Sajdl, P. Fitl, V. Švorčík, *Appl. Surf. Sci.* **283**, 438 (2013)
- J. Heitz, R.A. Barb, P. Sajdl, V. Svoř, 339, 144 (2015)
- R. Estevam-Alves, P.H.D. Ferreira, A.C. Coatrini, O.N. Oliveira, C.R. Fontana, C.R. Mendonca, *Int. J. Mol. Sci.* **17**, (2016)
- M.R. Kasaai, J. Arul, S.L. Chin, G. Charlet, *J. Photochem. Photobiol. A Chem.* **120**, 201 (1999)
- M.R. Kasaai, S.L. Chin, J. Arul, *J. Photochem. Photobiol. A Chem.* **159**, 207 (2003)
- S. Gaspard, M. Oujja, R. de Nalda, C. Abrusci, F. Catalina, L. Bañares, M. Castillejo, *Appl. Surf. Sci.* **253**, 6420 (2007)
- S. Gaspard, M. Oujja, R. De Nalda, C. Abrusci, F. Catalina, L. Baneres, S. Lazare, M. Castillejo, *Appl. Surf. Sci.* **254**, 1179 (2007)
- P.E. Dyer, R. Srinivasan, *Appl. Phys. Lett.* **48**, 445 (1986)
- O. Kermani, H. Lubatschowski, *Fortschr. Ophthalmol.* **88**, 748 (1991)
- A.G. Doukas, T.J. Flotte, *Ultrasound Med. Biol.* **22**, 151 (1996)
- L.D. Landau, E.M. Lifshitz, J.B. Sykes, W.H. Reid, E.H. Dill, *Phys. Today* **13**, 44 (1960)
- I. Itzkan, D. Albagli, M.L. Dark, L.T. Perelman, C.V. Rosenberg, M.S. Feld, *PNAS* **92**, 1960 (1995)
- D. Albagli, M. Dark, C. von Rosenberg, L. Perelman, I. Itzkan, M.S. Feld, *Med. Phys.* **21**, 1323 (1994)
- J.N. Goodier, *Philos. Mag.* **23**, 1017 (1937)
- G. Paltauf, P.E. Dyer, *Chem. Rev.* **103**, 487 (2003)
- S. Lazare, I. Elaboudi, M. Castillejo, A. Sionkowska, *Appl. Phys. A Mater. Sci. Process.* **101**, 215 (2010)
- Y. Dong, Y. Ruan, H. Wang, Y. Zhao, D. Bi, *J. Appl. Polym. Sci.* **93**, 1553 (2004)
- K. Sakurai, T. Maegawa, T. Takahashi, *Polymer (Guildf)*. **41**, 7051 (2000)
- P.G. Gobbi, F. Carones, R. Brancato, R. Pini, S. Siano, *Eur. J. Ophthalmol.* **5**, 275 (1995)
- F.W. Cross, R.K. Al-Dhahir, P.E. Dyer, A.J. MacRobert, *Appl. Phys. Lett.* **50**, 1019 (1987)
- S. Gaspard, M. Oujja, R. de Nalda, C. Abrusci, F. Catalina, L. Bañares, S. Lazare, M. Castillejo, *Appl. Surf. Sci.* **254**, 1179 (2007)
- S. Prez, E. Rebollar, M. Oujja, M. Martn, M. Castillejo, *Appl. Phys. A Mater. Sci. Process.* **110**, 683 (2013)
- P.E. Dyer, C.D. Walton, K. Akeel, *Opt. Lett.* **30**, 1336 (2005)
- M. Castillejo, et al., *Appl. Phys. A* 719 (2008)
- Y. Huang, D.R. Paul, *J. Polym. Sci. Part B Polym. Phys.* **45**, 1390 (2007)
- A. Lazaridou, C.G. Biliaderis, *Carbohydr. Polym.* **48**, 179 (2002)